HIGH RESOLUTION MEASUREMENT OF INTERNAL FULL-FIELD DISPLACEMENTS AND STRAINS USING GLOBAL SPECTRAL DIGITAL VOLUME CORRELATION

F. Mortazavi[1], E. Ghossein[1], M. Levesque[1*] and I. Villemure[2,3]

[1]CREPEC, Department of Mechanical Engineering, Ecole Polytechnique de Montreal, Montreal, Canada
[2]Department of Mechanical Engineering, Ecole Polytechnique de Montreal, Montreal Canada
[3]Research Center, Sainte-Justine University Hospital, Montreal, Canada
*corresponding author: martin.levesque@polymtl.ca

Keywords: *Digital Volume Correlation, Full-field measurements, micro-scale strain, composites, Fast Fourier Transform, Global Approach*

1 Introduction

The Digital Image Correlation (DIC) technique has established itself as an important tool in the area of experimental mechanics for more than three decades [1]. The valuable knowledge on the full-field displacements and strains that the technique provides in 2D has paved the way for interesting applications, such as mechanical properties [2, 3], strain mapping [4], etc. The theoretical framework of DIC can be expanded into three dimensions, in which case it is called Digital Volume Correlation (DVC) [5]. DVC has found emerging applications in the past decade [5–7] concurrently with the advances made in 3D imaging technologies, such as X-ray tomography and confocal microscopy. DVC allows for non-destructively evaluating displacements and strains *inside* materials. The first developments of DVC were based on local approaches [5, 8]. Later, global approaches were developed based on trilinear Finite Element (FE) shape functions [9], as well as enriched FE shape functions for specimens containing cracks [10]. However, as a result of the extension from 2D to 3D, the amount of data as well as the number of Degrees of Freedom (DOF) for DVC is significantly increased in both local and global approaches, when compared to their 2D counterparts. Consequently, DVC algorithms are highly demanding in terms of computer resources. This limitation has hindered the practical application of high-resolution DVC.

The present paper deals with the numerical aspects of DVC, specifically as far as high-resolution DVC is concerned. We propose a global approach based on Fourier basis functions referred to as Improved Spectral DVC (IS-DVC) hereinafter. Being an extension to 3D of the Improved Spectral Approach (ISA) [11–13], IS-DVC makes use of Fast Fourier Transform (FFT) to convert the computationally cumbersome system of equations in Fourier domain to an explicit equation for the displacement field in the spatial domain. The expression thus found can be evaluated quite efficiently. The interesting feature of the approach lies in the fact that the complexity of the correlation procedure does not significantly increase for larger number of DOF.

2 Background
2.1 Concept of pattern matching

Let $f(\mathbf{x})$ and $g(\mathbf{x})$ represent the intensity functions of spatial coordinates $\mathbf{x} = (x, y, z)$ corresponding to the undeformed and deformed images, respectively. In ideal conditions, these two configurations are correlated through a mapping of coordinates expressed by the following relation:

$$f(\mathbf{x}) = g(\check{\mathbf{x}}) \quad \text{where} \tag{1a}$$
$$\check{\mathbf{x}} = \mathbf{x} + \mathbf{u}_{\text{exact}}(\mathbf{x}) \tag{1b}$$

where $\mathbf{u}_{\text{exact}}(\mathbf{x})$ is the displacement vector field resulting from the applied loads. The exact displacement, in the Volume of Interest (VOI), is estimated by a mathematical function with specified Degrees of Freedom

(DOF), i.e.:

$$\mathbf{u}_{\text{exact}}(\mathbf{x}) \approx \mathbf{u}(\mathbf{x}; \mathbf{p}) \quad (2)$$

where $\mathbf{p}$ is the set of parameters representing the DOF that should be determined from pattern matching. The pattern matching consists in finding the parameters that minimize the gap between $f(\mathbf{x})$ and $g(\breve{\mathbf{x}})$. This can be expressed as follows:

$$\mathbf{p_{opt}} = \operatorname*{argmin}_{\mathbf{p} \in \mathcal{A}} \left\{ \int_{\text{VOI}} [f(\mathbf{x}) - g(\mathbf{x} + \mathbf{u}(\mathbf{x}; \mathbf{p}))]^2 \, d\mathbf{x} \right\} \quad (3)$$

where $\mathcal{A}$ denotes the set of admissible choices for $\mathbf{p}$ and the integrand is called the *squared correlation residuals* that should be minimized. For the sake of simplicity, the above formulation is written assuming the intensity functions are continuous, hence the use of integral operators. In practice, the discrete image functions are interpolated using proper interpolation methods [14–16] in order to perform the optimization at sub-pixel positions.

2.2 Resolution strategy

Different approaches of DIC depend, in the first place, on how the sought displacement field is formulated. Nevertheless, no matter how it is formulated, the displacement fields for different approaches can be expressed as the linear combination of several chosen basis functions [17], which can be expressed in the form of the following vector product:

$$\mathbf{u}(\mathbf{x}; \mathbf{p}) = \begin{bmatrix} \psi_1(\mathbf{x}) & \psi_2(\mathbf{x}) & \cdots & \psi_K(\mathbf{x}) \end{bmatrix} \begin{bmatrix} \boldsymbol{v}_1 \\ \boldsymbol{v}_2 \\ \vdots \\ \boldsymbol{v}_K \end{bmatrix} \quad (4a)$$

$$\text{where} \quad \mathbf{p} \equiv \{ \boldsymbol{v}_n | n = 1, 2, \cdots, K \} \quad (4b)$$

$\boldsymbol{v}_n$ are the sequence of unknown 3×1 (or 2×1 in DIC) vectors associated with basis functions $\psi_n(\mathbf{x})$ and K is the total number of basis functions. Except for some approaches (for example in [18]), a Newton iterative strategy is often used to solve the problem (3). The iterations start with an initial solution $\mathbf{p}^{(0)}$ (leading to $\mathbf{u}^{(0)}$), at iteration i, $g(\mathbf{x} + \mathbf{u})$ is corrected for

$\mathbf{u}^{(i-1)}$ and the new solution lies in finding the increment $\delta\mathbf{u}^{(i)} = \mathbf{u}^{(i)} - \mathbf{u}^{(i-1)}$. It is assumed that the sought increment, $\delta\mathbf{u}^{(i)}$, is small enough so that one can linearize $g\left(\mathbf{x} + \mathbf{u}^{(i-1)}(\mathbf{x}) + \delta\mathbf{u}(\mathbf{x})\right)$ as:

$$g\left(\mathbf{x} + \mathbf{u}^{(i-1)}(\mathbf{x}) + \delta\mathbf{u}(\mathbf{x})\right) \approx \quad (5a)$$
$$g\left(\mathbf{x} + \mathbf{u}^{(i-1)}(\mathbf{x})\right) + \nabla_{\mathbf{x}}^T g\left(\mathbf{x} + \mathbf{u}^{(i-1)}(\mathbf{x})\right) \delta\mathbf{u}(\mathbf{x})$$

$$\text{provided that } \forall \mathbf{x}, \, \|\delta\mathbf{u}(\mathbf{x})\| < \|\boldsymbol{\eta}\|. \quad (5b)$$

where $\boldsymbol{\eta}$ is a small real vector, $\nabla_{\mathbf{x}}$ denotes the gradient operator with respect to vector $\mathbf{x}$, and $\square^T$ indicates the vector transpose. Therefore, the First-order Optimality for the problem (3) is written as:

$$\nabla_{\boldsymbol{v}_n} \left[\int_{\text{VOI}} \left[f(\mathbf{x}) - \breve{g}^{(i-1)}(\mathbf{x}) \right. \right.$$
$$\left. \left. - \nabla_{\mathbf{x}}^T \breve{g}^{(i-1)}(\mathbf{x}) \delta\mathbf{u}(\mathbf{x}; \mathbf{p}) \right]^2 d\mathbf{x} \right]$$
$$= \mathbf{0} \quad n = 1, 2, \cdots, K \quad (6)$$

and

$$\breve{g}^{(i)}(\mathbf{x}) = g\left(\mathbf{x} + \mathbf{u}^{(i)}(\mathbf{x})\right) \quad (7)$$

By applying the differentiation and after simplifications, equation (6), is turned into a system of linear equations:

$$\begin{bmatrix} \mathbf{J}_{11} & \mathbf{J}_{12} & \cdots & \mathbf{J}_{1K} \\ \mathbf{J}_{21} & \ddots & & \vdots \\ \vdots & & \ddots & \vdots \\ \mathbf{J}_{K1} & \cdots & \cdots & \mathbf{J}_{KK} \end{bmatrix} \begin{bmatrix} \boldsymbol{v}_1 \\ \boldsymbol{v}_2 \\ \vdots \\ \boldsymbol{v}_K \end{bmatrix} = \begin{bmatrix} \boldsymbol{\rho}_1 \\ \boldsymbol{\rho}_2 \\ \vdots \\ \boldsymbol{\rho}_K \end{bmatrix} \quad (8a)$$

where $\mathbf{J}_{mn}$ and $\boldsymbol{\rho}_m$ are 3×3 (or 2×2) and 3×1 (or 2×1) matrices calculated from the following equations:

$$\mathbf{J}_{mn} = \int_{\text{VOI}} \left(\left(\nabla_{\mathbf{x}} \breve{g}^{(i-1)} \otimes \nabla_{\mathbf{x}} \breve{g}^{(i-1)} \right)(\mathbf{x}) \right.$$
$$\left. \times \psi_m(\mathbf{x}) \psi_n(\mathbf{x}) \right) d\mathbf{x} \quad (8b)$$

$$\boldsymbol{\rho}_m = \int_{\text{VOI}} \left(\left(f(\mathbf{x}) - \breve{g}^{(i-1)}(\mathbf{x}) \right) \right.$$
$$\left. \times \psi_m(\mathbf{x}) \nabla_{\mathbf{x}} \breve{g}^{(i-1)}(\mathbf{x}) \right) d\mathbf{x} \quad (8c)$$

respectively, and $\otimes$ denotes the dyadic product. Equation (8a) is considered as the governing equation for the gradient-based pattern matching.

2.3 Spectral approach

Roux et al. [13] and Wagne et al. [12] introduced a very appealing approach based on the Fourier decomposition of the sought displacement field in 1D and 2D, respectively. In this framework, the displacement field was expressed as:

$$\mathbf{u}(\mathbf{x}) = \sum_n \boldsymbol{v}_n \exp(\hat{\imath} \boldsymbol{\omega}_n \cdot \mathbf{x}) \qquad (9a)$$

where

$$\boldsymbol{\omega}_n \in \left\{ \left(\frac{p\pi}{L}, \frac{q\pi}{L} \right) \middle| \begin{array}{c} n = 2Mq + p \\ p, q \in \mathbb{Z} \\ -M \leq p, q \leq M - 1 \end{array} \right\}, \qquad (9b)$$

L denotes the half-width of the Region of Interest (ROI) and $M \leq L$ implies that only Fourier coefficients within a square of size $2M \times 2M$ were used to estimate the displacement field (i.e. $K = 4M^2$). In the extreme case where this square extends over the whole ROI size (i.e. $M = L$), the displacement field is aimed to be exactly reconstructed. However, this is not possible due to the ill-posed nature of the inverse problem. In their study, Wagne et al. [12] showed that $M \ll L$ in order for the approach to lead to meaningful results. It is easy to show that with the chosen formulation, matrix elements of the governing equation, i.e. equations (8b) and (8c), turn into the following Fourier transforms:

$$\mathbf{J}_{mn} = \mathcal{F} \left\{ \left(\nabla_{\mathbf{x}} \breve{g}^{(i-1)} \otimes \nabla_{\mathbf{x}} \breve{g}^{(i-1)} \right) \right\}_{[-m-n]}$$
$$:= \widetilde{\mathbf{J}}_{[-m-n]} \quad (10a)$$

$$\boldsymbol{\rho}_m = \mathcal{F} \left\{ \left(f - \breve{g}^{(i-1)} \right) \nabla_{\mathbf{x}} \breve{g}^{(i-1)} \right\}_{[-m]}$$
$$:= \widetilde{\boldsymbol{\rho}}_{[-m]} \quad (10b)$$

where the Fourier transform of a function $h(\mathbf{x})$ is defined as:

$$\mathcal{F} \{h\}_{[m]} = \int_{\mathrm{ROI}} h(\mathbf{x}) \exp\left(-\hat{\imath} \boldsymbol{\omega}_m \cdot \mathbf{x} \right) \mathbf{dx} \qquad (11)$$

(note that only the Fourier terms within the $2M \times 2M$ square are calculated in equations (10a) and (10b)). Therefore, equation (8a) can be written in the following form using the Einstein notation:

$$\widetilde{\mathbf{J}}_{[m-n]} \boldsymbol{v}_n = \widetilde{\boldsymbol{\rho}}_{[m]} \quad \text{summation over } n \qquad (12)$$

The left-hand side of the above equation is a convolution product. The main interest of the spectral approach lies in the fact that instead of directly solving equation (12) in the frequency domain, one may bring the calculations back to the spatial domain. Thus, the convolution operation turns into a simple matrix product in the real space. In doing so, equation (12) is transformed to the following practical form:

$$\left(\left(\widehat{\nabla_{\mathbf{x}} \breve{g} \otimes \nabla_{\mathbf{x}} \breve{g}} \right)^{(i-1)} \cdot \delta \mathbf{u}^{(i)} \right) (\mathbf{x}) =$$
$$\left(\widehat{(f - \breve{g}) \nabla_{\mathbf{x}} \breve{g}} \right)^{(i-1)} (\mathbf{x}) \quad (13)$$

where $\widehat{\square}$ denotes low-pass filtering in the frequency domain by preserving only $2M \times 2M$ coefficients. One faces here a 2×2 linear algebraic system for each point in the space. Such a system is analytically solved giving rise to two explicit expressions for the estimated displacement components. The main computational burden is performing a forward and a backward FFT to apply the Fourier low-pass filtering.

Wagne et al. [12] used multiscale iterations for large displacement magnitudes [19]. The developed strategy showed high reconstruction capacities while having drastically low computational costs. However, their approach suffered from a limitation stemming from the periodic nature of the utilized basis functions, i.e. the approach highly relied on periodic displacement fields and periodic images; a condition that is rarely met in real experiments. Meanwhile, this limitation was shown to be alleviated in 1D by using prior displacement correction using measurements based on a linear displacement model [13] .

3 IS-DVC

In the IS-DVC, the 2D framework of the spectral approach is extended to 3D while improving on the accuracy and the functionality of the approach for practical

applications. These improvements were completely elaborated in the ISA [11] by the authors and will be briefly formulated here in 3D. The number of DOF of the sought displacement field in the spectral approach, equation (9a), was determined by K (total number of basis functions). Alternatively, it can be considered as a box lowpass filter, which passes only $2M \times 2M$ basis functions. In the ISA [11], this filter was replaced with a Gaussian filter, which was shown to significantly improve the accuracy of the measurements. Considering the Gaussian filter as:

$$H_n^{(\kappa)} = \exp\left(-\frac{L^2 \|\boldsymbol{\omega}_n\|^2}{2\pi^2 \kappa^2}\right), \qquad (14)$$

the sought displacement field is expressed in the following form:

$$\mathbf{u}(\mathbf{x}) = \sum_n H_n^{(\kappa)} \boldsymbol{v}_n \exp\left(\hat{\imath}\boldsymbol{\omega}_n \cdot \mathbf{x}\right) \qquad (15)$$

$$\boldsymbol{\omega}_n \in \left\{\left(\frac{p\pi}{L}, \frac{q\pi}{L}, \frac{s\pi}{L}\right) \,\middle|\, \begin{array}{c} n = 4L^2 s + 2Lq + p \\ p, q, s \in \mathbb{Z} \\ -L \leq p, q, s \leq L - 1 \end{array}\right\} \qquad (16)$$

where κ is the cutoff wavenumber corresponding to the Gaussian filter. Since the formulation of IS-DVC is defined in 3D, $\mathbf{u}$, $\boldsymbol{v}_n$ and $\boldsymbol{\omega}_n$ are all 3×1 vector fields and the VOI contains $2L \times 2L \times 2L$ voxels. Similar to the spectral approach, one should have $\kappa \ll L$ to ensure the accuracy of the results [11]. Proceeding with the improved formulation, one obtains the same governing equation (13) as obtained in the spectral approach. Here, $\widehat{\Box}$ denotes low-pass filtering in the frequency domain using the mask $H^{(\kappa)}$. As in the ISA [11], the following modification, inspired by the Hessian modification in nonlinear optimization [20], ensures that the modified dyadic tensor is always positive definite:

$$\forall \mathbf{x}, \quad \mathbf{B}^{(i)}(\mathbf{x}) := \left(\widehat{\nabla_\mathbf{x} \breve{g} \otimes \nabla_\mathbf{x} \breve{g}}\right)^{(i)}(\mathbf{x}) + \tau^{(i)}(\mathbf{x})\mathbf{I} \qquad (17)$$

where $\mathbf{I}$ is the identity tensor and τ is defined as:

$$\tau^{(i)}(\mathbf{x}) = \max\left\{0, \delta_0 - \lambda_1^{(i)}(\mathbf{x})\right\} \qquad (18)$$

where δ_0 is a positive real number (typical value 10^{-2}) and $\lambda_1^{(i)}(\mathbf{x})$ denotes the smallest eigenvalue of the

dyadic tensor field at iteration i. Therefore, equation (13) is modified into the following equation:

$$\left(\mathbf{B}^{(i-1)} \cdot \delta\mathbf{u}^{(i)}\right)(\mathbf{x}) = \left(\widehat{(f - g)\nabla_\mathbf{x} \breve{g}}\right)^{(i-1)}(\mathbf{x}) \qquad (19)$$

Provided that δ_0 is small compared to the average values of λ_1, the resulting displacements are meaningful enough to reduce the dissimilarity objective, equation (3). Equation (19) is evaluated in 3D. The analytical solution to the 3×3 linear system (19) leads to three explicit expressions for the displacement components that can be evaluated for every voxel. Aside from the additional computational burden dictated by the 3D operations (e.g. 3D-DFT, arithmetic operations and sub-pixel interpolation), the solution to the above 3×3 system involves considerably higher number of operations when compared to the 2×2 version in 2D. However, these operations are performed sequentially and therefore can be carried out efficiently. Moreover, thanks to the FFT advantages, the 3D-DFT operations can be also performed with drastically less computational efforts, thus making the algorithm suitable for 3D applications.

In the iterative procedure, the cutoff wavenumber, κ, was also gradually increased so that it reached its presumed value at final iterations, thus correcting for low-frequency terms in the displacement before proceeding to compute the high-frequency terms. Therefore, at iteration i, the displacement field $\mathbf{u}^{(i)}$ was corrected as:

$$\mathbf{u}^{(i)} = \mathbf{u}^{(i-1)} + \delta\mathbf{u}^{(i,\kappa)} \qquad (20)$$

where $\delta\mathbf{u}^{(i,\kappa)}$ was calculated from equation (19) using te current value of κ. The algorithm decides to augment κ when the Root Mean Square (RMS) of the correction $\delta\mathbf{u}^{(i,\kappa)}$, denoted by $\sigma_{\delta\mathbf{u}}$, becomes inferior to 10^{-3}. This criterion is referred to as the stagnation measure. A slight variation with respect to the ISA was used herein to systematically stop the algorithm. The criterion was based on the observed trend of the reduction in $\sigma_{\delta\mathbf{u}}$ as a function of κ, which is illustrated in Fig. 1 As seen from the trend, there is a jump in $\sigma_{\delta\mathbf{u}}$ as a result of an increase in κ, which is due to the increased DOF in the sought displacement field allowing for more variations (hence a higher RMS) and probably a more
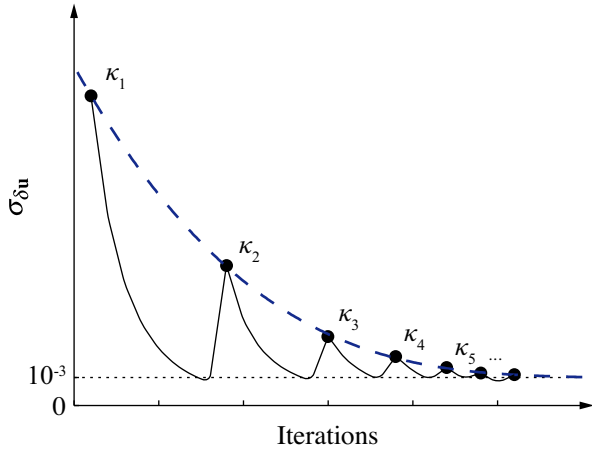
Fig. 1: Illustration of the general trend of $\sigma_{\delta\mathbf{u}}$ as a function of iterations. The jumps correspond to an increase of κ due to the fulfillment of the stagnation measure. It can be seen that these jumps decrease logarithmically, as illustrated by the dashed line.

enriched reconstruction. However, this jump decreases with a quasi-logarithmic decay as κ increases, which means that the added DOF have less impact on the accuracy of the measurement. Thus, there is a risk that the κ-induced reduction of the uncertainty is overlaid by noise- and interpolation-induced errors. Therefore, the algorithm was set to stop when $\sigma_{\delta\mathbf{u}}$ at the jump corresponding to κ became inferior to 10^{-3} (see [11] for further details on the algorithm).

3.1 Other variations with respect to ISA

3.1.1 Prior correction for non-periodic displacements

The major utility of a two-fold correlation, is to remove the limitation imposed by the Fourier-based decomposition of the displacement field in the spectral approach. This was shown by Roux et al. [13] and Mortazavi et al. [11] to efficiently operate for non-periodic images and displacement fields, in 1D and 2D, respectively. In the ISA [11], the authors used a local approach followed by 2D surface fitting to roughly estimate the non-periodic part of the displacement field. However, due to the additional computational burden associated with the surface fitting algorithm, and for the sake of simplicity in the evaluation of the presented examples, a global approach based on an affine transformation for the formulation of the non-periodic part of the displace-

ment field was considered (as previously done in [13] for 1D images). In doing so, the initial solution $\mathbf{u}^{(0)}$ in IS-DVC is of the following form:

$$\mathbf{u}^{(0)} = (\mathbf{R_0} + \mathbf{E_0}) \cdot \mathbf{x} + \mathbf{t_0} \tag{21}$$

where $\mathbf{R_0}$ and $\mathbf{E_0}$ are the homogeneous rotation and strain tensors, respectively, and $\mathbf{t_0}$ is the rigid body translation vector. The transform involves 12 DOF, which are found by solving the pattern matching problem (**??**) through nonlinear optimization.

4 Simulated experiments

Three complex artificial experiments were performed to evaluate the functionality of IS-DVC. In all experiments, 8-bit 128^3 voxel synthetic volume images were artificially transformed to a priori known deformed states using displacement fields simulated from mechanical analyses (referred to as exact displacement fields hereinafter). The synthetic images were generated using the Fractals theory, namely, "Brownian motion" [21]. This choice allowed for fast generation of 3D images with random but correlated 3D textures. Fig. 2 shows a typical volume image used in this study. The root mean square of the error between the measured quantities (displacement/strain) and their exact values was calculated as the measurement uncertainty of the corresponding quantity. To this end, the measured values within 10 voxels near the volume edges were excluded from the calculation to avoid any boundary errors. In the first two examples, two different composite geometries were considered, namely, a matrix reinforced by randomly distributed spherical particles in the first case (example I) and in the second case, by randomly distributed ellipsoidal fibers (example II). To this end, an in-house MATLAB code from another study by the authors [22] was used to generate the mentioned random microstructures for any given size and volume fraction. The geometries are illustrated in Fig. 4(a) and 5(a). The elastic response of the obtained microstructures under 2% applied compressive strain in z direction was subsequently calculated using an FFT-based numerical method [23]. Table 1 lists the properties used for generating the artificial data (geometry and mechanical properties) for both composites. In the third example, a displacement field with a discontinuity was considered, namely, that of the analytical
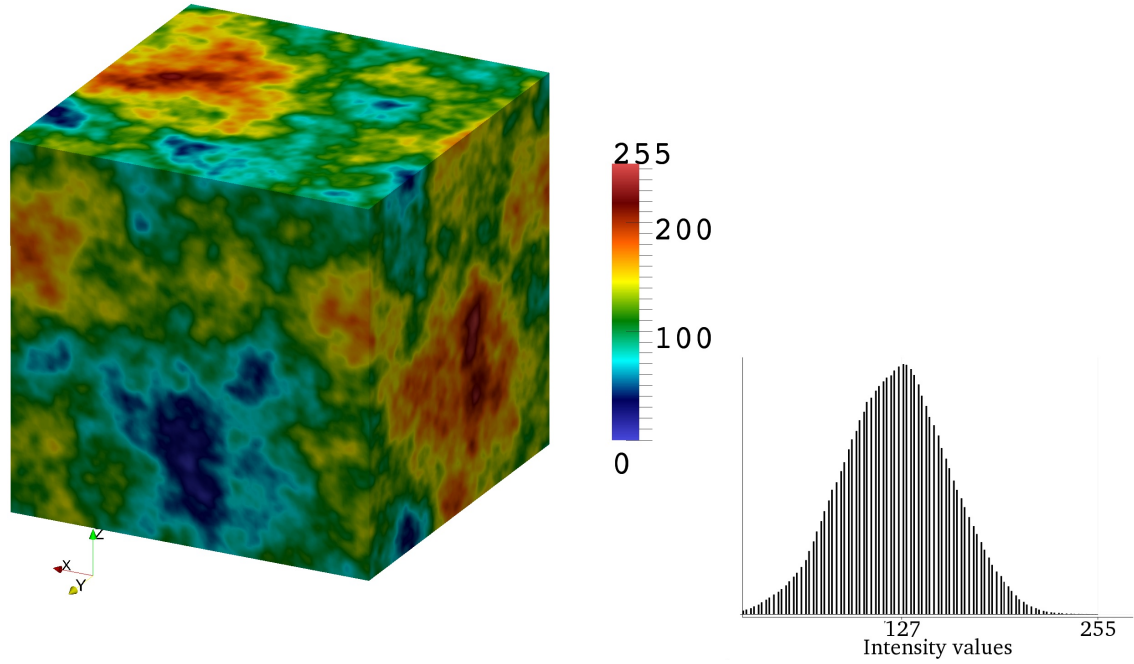
Fig. 2: Synthetic grayscale volume image ($128 \times 128 \times 128$ voxels, 8-bit) used for the artificial experiments as well as its histogram. A different colormap was used here for illustrative purposes.

Table 1: Properties used for the generation of composites with spherical (example I) and ellipsoidal particles (example II) used in the artificial experiments. Subscripts m and p refer to matrix and particle, respectively. E denotes the elastic modulus and ν is the poisson ratio. The particle volume fraction is denoted by v.f.

	E_m (GPa)	E_p (GPa)	ν_m	ν_p	v.f.(%)	aspect ratio	size ratio ($d^{\dagger} = L/r$)
Example I	25	5	.2	.3	10	1	2.5
Example II	50	5	.2	.3	5	20	16

$^{\dagger}d$ is defined as the ratio of image half-length (L) to the smallest particle radius (r), which gives an estimation of the particle voxel-size in the volume image (see section 5).

mode I 2D crack. This example is interesting in the sense that the discontinuous displacement field requires a large number of DOF (high frequency bases) to be approximated with a continuous displacement field expressed as per a Fourier expansion. This example is useful to assess the potentials and limitations of the presented approach. It should be noted that the accurate measurement of discontinuous displacement fields is not within the scope of the present approach as it would require further considerations to deal with such cases. The reader is referred to other approaches specifically tailored for cracked specimens [10, 24, 25]. We used the following discontinuous function for the z-component

of the preset displacement field, w, according to the theory of linear elastic fracture mechanics:

$$w(x, r, \theta) = C_{\mathrm{I}}\sqrt{r}\left[\left(\eta + \frac{1}{2}\right)\sin\frac{\theta}{2} - \frac{1}{2}\sin\frac{3\theta}{2}\right]$$

(22)

where C_{I} and η are mechanical constants and (r, θ) are the polar coordinates centered at the crack tip in the yz plane (crack oriented along $\theta = \pi$).

The artificial transformations of the undeformed volume images were performed using the transformation of their Fourier series, hence avoiding any interpolation bias at this level of experiments. The tricubic B-spline

interpolation scheme [16] was used for sub-pixel measurement since it induces relatively small interpolation bias [11].

5 Results and discussion

5.1 Examples I and II: artificial composites

Fig. 3(a) and 3(c) show the evolution of displacement uncertainty as a function of the iterations, for both examples. The measurements stopped at $\kappa = 9$ and $\kappa = 10$ for examples I and II, respectively, according to the criteria of section 3. The evolution of these criteria are plotted in Fig. 3(b) and 3(d) as functions of the characteristic subset length introduced in [11] for ISA, i.e.:

$$\ell = \frac{2L}{\alpha\kappa} \qquad (23)$$
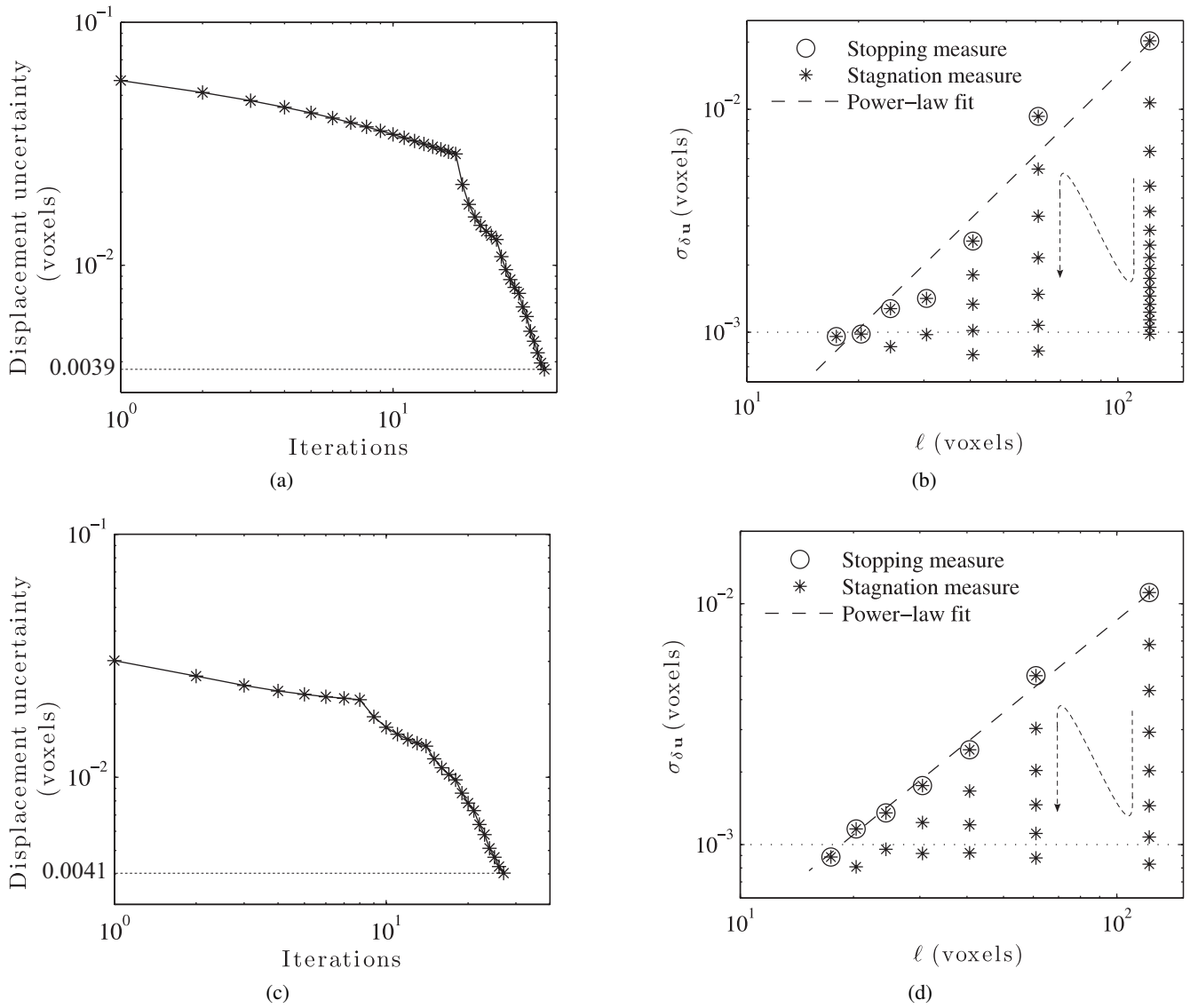
where ℓ is the characteristic subset length and $\alpha \approx 1.05 - 1.25$ ($\alpha = 1.05$ was used for the aforementioned plots). This parameter relates the cutoff wavenumber in the frequency domain to a more tangible measure of resolution in the spatial domain. As shown in these plots, at final iterations, the stopping criterion reached the value 10^{-3}, where the algorithm systematically stops. Also, one notes the power-law fit for the reduction trend of the stopping criterion, which confirms the validity of the notions discussed in section 3. It is worth noting that for every image correlation algorithm, successful measurements consist in achieving a balance between two divergent trends, namely, uncertainty reduction thanks to increasing number of DOF (i.e. smaller characteristic lengths) and uncertainty rise due the loss of intensity variations as a result of smaller characteristic lengths. In this sense, decision-making criteria, e.g. the stopping and stagnation measures herein, become key factors in the final accuracy of the measurements. The exact tradeoff point (i.e. the minimum uncertainty as a function of κ) for examples I and II was identified as 0.0034 and 0.0038 voxels, respectively, ocurring at $\kappa = 11$ for both cases. These values were obtained by deactivating the stopping criterion to let the iterations continue for higher values of κ and to see at what point the minimum uncertainty occurs. Comparing these values to the uncertainties at the final iterations shown in Fig. 3(a) and 3(c), one concludes that the iterations stopped very close to the tradeoff point, hence

confirming the suitability of the devised criteria.

Fig. 4 and 5 contain volume representations of some measurement results for examples I and II, respectively. The correlation residuals (Fig. 4(f) and 5(f)) ranging between -0.5 and 0.5 (in the dynamic range scale of the original images) imply that satisfactory correlations have been established between the undeformed and deformed states. Fig. 4 and 5(d)-(e) show the calculated ε_{zz} strain (exact and measured) mapped on the deformed state of the volume. The measured strains reveal a significant similarity to the exact simulated strains, which means that IS-DVC was successfully capable of capturing the strain heterogeneities through the volume. This can be better perceived from Fig. 4 and 5(b)-(c) , which represent the thresholded ε_{zz} strains in the particles with threshold values -1.6% and -1.3%, respectively. These values were chosen according to the statistical distribution of the exact strain using "simple thresholding" (e.g. `graythresh` in MATLAB). One recognizes a close estimation of the shape and the orientation of the particles from their thresholded measured strain, when compared to the exact strain as well as the original geometry. Table 2 gives the measured strains uncertainties as well as the mean strain values (denoted by a bar) within individual phases for the two examples. The uncertainty of the ε_{zz} strain within the particle (p) or matrix (m) is denoted by $\delta\varepsilon_{zz}^{p/m}$ and is calculated as the following:

$$\delta\varepsilon_{zz}^q = \sqrt{\frac{\sum_{i \in \Omega_q} \left(\varepsilon_{zz}^{\text{measured}}(\mathbf{x}^{\langle i \rangle}) - \varepsilon_{zz}^{\text{exact}}(\mathbf{x}^{\langle i \rangle})\right)^2}{N_q}}$$
$$(24)$$

where Ω_q denotes the ensemble of the regions containing the voxels of the individual phase q, and N_q is the total number of voxels in that region. One notes higher uncertainties within the particle, which is due to the abrupt changes of the strain in the vicinity of this phase. Nevertheless, this uncertainty is lower in the case of composite with spherical particles. This is mainly due to the lower elastic modulus contrast as well as the larger particle size (lower size ratio) of the spheres, when compared to those of the ellipsoids. The former reduces the heterogeneity of the strain while the latter increases the displacement resolution within the particles.

(a)

(b)

(c)

(d)

Fig. 3: Trend of displacement uncertainty as a function of iterations (a and c) and trend of $\sigma_{\delta \mathbf{u}}$ as a function of characteristic subset length ℓ (b and d) for examples I and II, respectively.

Table 2: Strain uncertainties as well as strain averages within individual phases for examples I and II: Comparison of averages with the exact strains.

	κ	$\bar{\varepsilon}_{zz}^{m}$	$\delta\varepsilon_{zz}^{m}$	$\bar{\varepsilon}_{zz}^{p}$	$\delta\varepsilon_{zz}^{p}$
Artificial composite with spherical particles					
IS-DVC measurements	9	-0.0230	0.0017	-0.0130	0.002
Simulation results (preset values)	NA	-0.0231		-0.0127	
Artificial composite with non-aligned quasi-cylindrical fibers					
IS-DVC measurements	10	-0.0206	0.0018	-0.0070	0.0035
Simulation results (preset values)	NA	-0.0207		-0.0065	
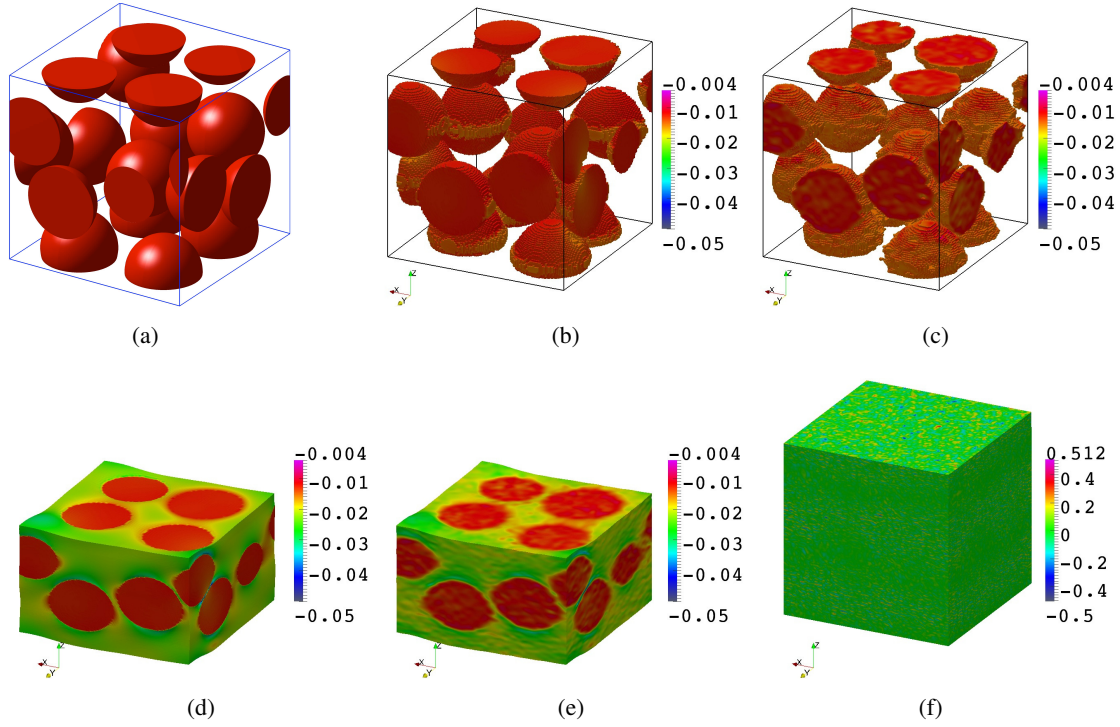
Fig. 4: (a) Geometry of the artificial composite with spherical particles (b) thresholded exact strain ε_{zz} with threshold value = 1.6% (c) thresholded measured strain ε_{zz} with the same threshold value as that of (b) (d) exact strain ε_{zz} image mapped on the deformed volume (according to the exact displacement field) (e) measured strain ε_{zz} image mapped on the deformed volume (according to the measured displacement field) (f) correlation residuals for the resulted measurements values are in the scale of the image dynamic range.

It is possible to derive a quantitative measure of proper particle size ratio with respect to the cutoff wavenumber κ using the characteristic subset length. In order for IS-DVC to be able to best estimate the strain within the particle, the particle's (smallest) radius, r, should be larger than the characteristic subset length, i.e.

$$r > \frac{2L}{\alpha\kappa} \quad \text{or} \quad \kappa > \beta d \qquad (25)$$

where $d = L/r$ is the particle size ratio (see Table 1) and $\beta = 2/\alpha \approx 1.6 - 1.9$. On this basis, κ_{min} for the spherical particles turned out to be 5 while this value for the elliptical particles was $25 \sim 30$. Obviously, we did not reach this value for the ellipsoidal particles due to the insufficient intensity variations associated to the 3D texture of the volume image. The above quantitative measure allows one to determine the feasibility of high-resolution measurements for a given composite geometry according to the particle size (in voxels) within the image.

5.2 Example III: crack displacement field

For the third example, the algorithm stopped at $\kappa = 13$. This means that higher DOF had larger impact on the uncertainty reduction, when compared to the two previous examples, which is not surprising since a discontinuous displacement field should be estimated. The measurements for $w(\mathbf{x})$ along a vertical line containing the discontinuity is plotted for $\kappa = 3$ and $\kappa = 13$ and compared to the exact plot in Fig. 7. As seen from the plot, for $\kappa = 13$, the displacement errors were rapidly damped for regions away from the discontinuity. Fig. 6 shows the volume image of the displacement field $w(\mathbf{x})$ compared to the exact displacement. A close agreement between the measured and the exact displacements can be observed, especially for regions far from the crack
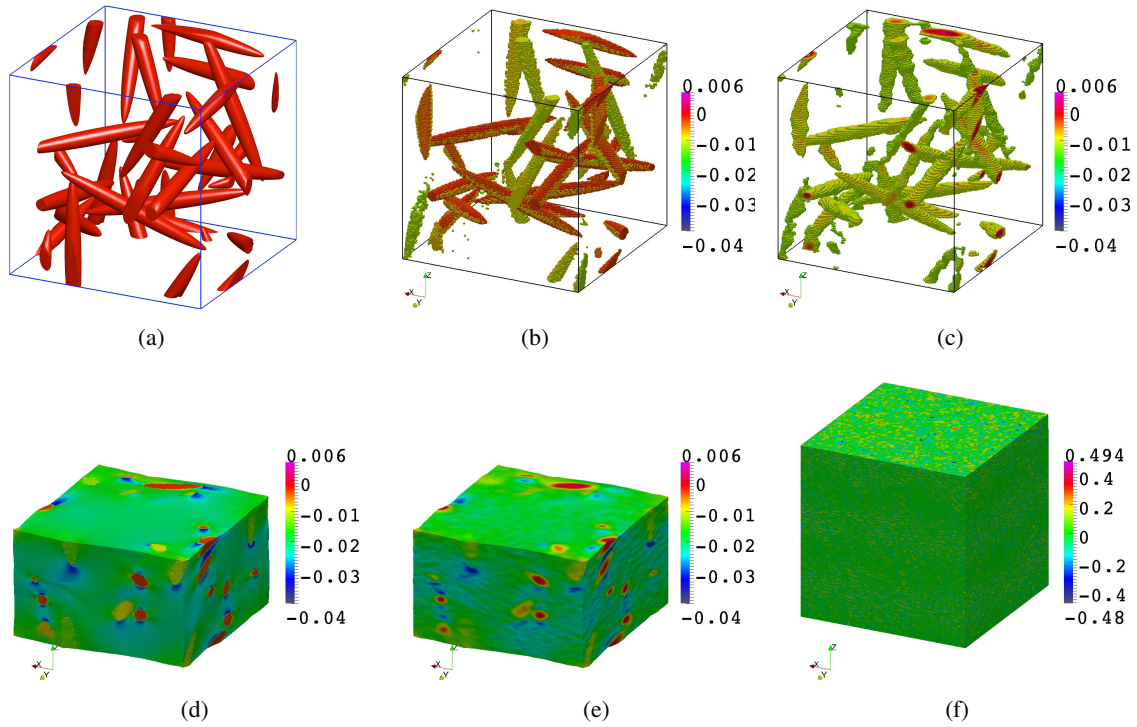
Fig. 5: (a) Geometry of the artificial composite with elliptical particles (b) thresholded exact strain ε_{zz} with threshold value = 1.3% (c) thresholded measured strain ε_{zz} with the same threshold value as that of (b) (d) exact strain ε_{zz} image mapped on the deformed volume (according to the exact displacement field) (e) measured strain ε_{zz} image mapped on the deformed volume (according to the measured displacement field) (f) correlation residuals for the resulted measurements values are in the scale of the image dynamic range.
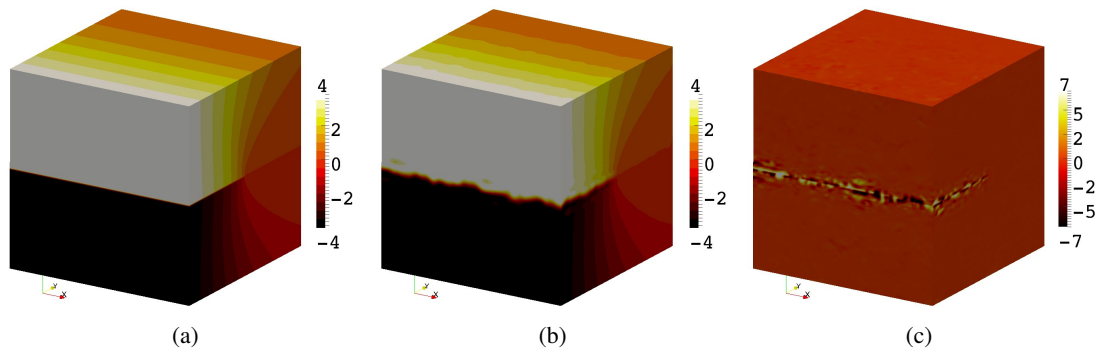
Fig. 6: (a) Exact displacement field in z direction for the analytical mode I crack (b) measured displacement field (c) correlation residuals, values are in the scale of image dynamic range

surface. The displacement uncertainty excluding the cracked region (10 voxels all around the crack) was .006 voxels, which is very acceptable, when compared to the other examples (Fig. 3). The correlation residuals for this examples (Fig. 6(c)) demonstrates how well the algorithm has succeeded to correlate the undeformed and deformed images. Obviously, there are significant residuals in the crack region, which means that the algorithm underperformed in this area. The presented example reveals that such discontinuities have
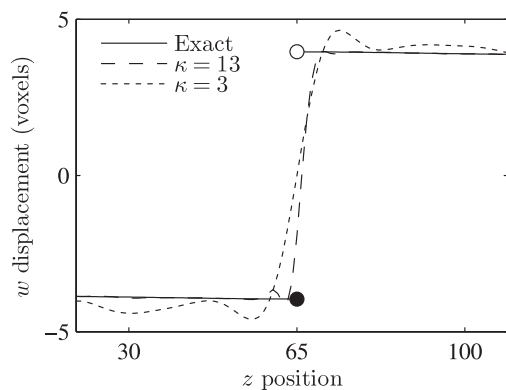
Fig. 7: Behavior of the measured displacement in the vicinity of the discontinuity for example III

very little effects on the accuracy of the measurements sufficiently far from the crack.

6 Conclusion

We proposed a global approach for fast and accurate high-resolution DVC. The approach was an extension to 3D of the 2D ISA based on a Fourier decomposition for the sought displacement field. Several artificial experiments were performed to evaluate the functionality of the IS-DVC for high resolution displacement measurements. Especially, two artificial composites were generated with spherical and quasi-cylindrical non-aligned particles to simulate the artificial experiments using synthetic images. The measurements on the composites were proven to be very successful in capturing strain heterogeneities through the volume with acceptable uncertainties, both in displacements and strains. Stopping and stagnation measures devised in the IS-DVC algorithm were shown to be very efficient in systematically stopping the iterations, hence adding to the robustness of the whole measurement process. Using the notion of characteristic subset length previously introduced in [11], a quantitative measure was derived to estimate the proper particle voxel-size for accurate capturing of strain heterogeneities as a function of cutoff wavenumber defining the measurement resolution. This a priori knowledge would help better designing experimental parameters (e.g. magnification, imaging resolution, etc.) to obtain the best results from IS-DVC. Furthermore, a third artificial example dealt with the measurement of a discontinuous displacement

field of analytical mode I crack from linear elastic fracture mechanics. The resulted measurement uncertainties, although not very low in the vicinity of the discontinuity, turned out to be fairly acceptable (around 0.006 voxel) for regions further from the crack. This experiment assessed the stability of IS-DVC in dealing with discontinuities.

The results obtained in this study are very promising for high-resolution DVC thanks to the significantly low computational costs associated with IS-DVC. It should be noted, however, that this first step requires further studies to deal with experimental limitations such as noise and artifact effects, which may hinder the full exploitation of the approach if not taken into consideration.

References

1. M. Sutton, W. Wolters, W. Peters, W. Ranson, S. McNeill, Determination of displacements using an improved digital correlation method, Image and Vision Computing 1 (1983) 133 – 139.

2. M. Grédiac, The use of full-field measurement methods in composite material characterization: interest and limitations, Composites Part A: Applied Science and Manufacturing 35 (2004) 751 – 761.

3. G. Geymonat, S. Pagano, Identification of mechanical properties by displacement field measurement: A variational approach, Meccanica 38 (2003) 535–545.

4. J. Q. D. Fonseca, P. M. Mummery, P. J. Withers, Full-field strain mapping by optical correlation of micrographs acquired during deformation, Journal of Microscopy 218 (2005) 9–21.

5. B. Bay, T. Smith, D. Fyhrie, M. Saad, Digital volume correlation: three-dimensional strain mapping using x-ray tomography, Experimental Mechanics 39 (1999) 217 – 26.

6. F. Forsberg, C. R. Siviour, 3d deformation and strain analysis in compacted sugar using x-ray microtomography and digital volume correlation, Measurement Science and Technology 20 (2009) 095703 (8pp).

7. J. Réthoré, N. Limodin, J.-Y. Buffière, F. Hild, W. Ludwig, S. Roux, Digital volume correlation analyses of synchrotron tomographic images, The Journal of Strain Analysis for Engineering Design 46 (2011) 683–695.

8. E. Verhulp, B. V. Rietbergen, R. Huiskes, A three-dimensional digital image correlation technique for strain measurements in microstructures, Journal of Biomechanics 37 (2004) 1313 – 1320.

9. S. Roux, F. Hild, P. Viot, D. Bernard, Three-dimensional image correlation from x-ray computed tomography of solid foam, Composites Part A: Applied Science and Manufacturing 39 (2008) 1253 – 1265.

10. J. Réthoré, J.-P. Tinnes, S. Roux, J.-Y. Buffière, F. Hild, Extended three-dimensional digital image correlation (x3d-dic), C.R. Mecanique 336 (2008) 643–9.

11. F. Mortazavi, M. Lévesque, I. Villemure, Image-based continuous displacement measurements using an improved spectral approach, Strain (2013) 16 pages. Published on-line. DOI : 10.1111/str.12034.

12. B. Wagne, S. Roux, F. Hild, Spectral approach to displacement evaluation from image analysis, Eur. Phys. J. AP 17 (2002) 247–252.

13. S. Roux, F. Hild, Y. Berthaud, Correlation image velocimetry: A spectral approach, Applied Optics 41 (2002) 108–115.

14. T. M. Lehmann, C. Gönner, K. Spitzer, Survey: Interpolation methods in medical image processing, IEEE Transactions on Medical Imaging 18 (1999) 1049–1075.

15. M. Unser, A. Aldroubi, M. Eden, B-spline signal processing. i. theory, Signal Processing, IEEE Transactions on 41 (1993) 821 –833.

16. M. Unser, A. Aldroubi, M. Eden, B-spline signal processing. ii. efficiency design and applications, Signal Processing, IEEE Transactions on 41 (1993) 834 –848.

17. F. Hild, S. Roux, Comparison of local and global approaches to digital image correlation, Experimental Mechanics 52 (2012) 1503–1519.

18. C. Franck, S. Hong, S. Maskarinec, D. Tirrell, G. Ravichandran, Three-dimensional full-field measurements of large deformations in soft materials using confocal microscopy and digital volume correlation, Experimental Mechanics 47 (2007) 427 – 438.

19. G. Besnard, F. Hild, S. Roux, "finite-element" displacement fields analysis from digital images: Application to portevin-le châtelier bands, Experimental Mechanics 46 (2006) 789 – 803.

20. J. Nocedal, S. J. Wright, Numerical Optimization, Springer, 2000.

21. M. F. Barnsley, R. L. Devaney, B. B. Mandelbrot, D. Peitgen, R. F. Voss, The Science of Fractal Images, Springer-Verlag, Berlin, 1988.

22. E. Ghossein, M. Lévesque, A fully automated numerical tool for a comprehensive validation of homogenization models and its application to spherical particles reinforced composites, International Journal of Solids and Structures 49 (2012) 1387 – 1398.

23. H. Moulinec, P. Suquet, A numerical method for computing the overall response of nonlinear composites with complex microstructure, Computer Methods in Applied Mechanics and Engineering 157 (1998) 69 – 94.

24. E. Fagerholt, T. Borvik, O. Hopperstad, Measuring discontinuous displacement fields in cracked specimens using digital image correlation with mesh adaptation and crack-path optimization, Optics and Lasers in Engineering 51 (2013) 299 – 310.

25. J. Réthoré, F. Hild, S. Roux, Extended digital image correlation with crack shape optimization, International journal for numerical methods in engineering 73 (2008) 248–272.